

Hydrodynamical Response of a Circumbinary Gas Disk to Black Hole Recoil and Mass Loss

Lia R. Corrales¹, Zoltán Haiman¹, Andrew MacFadyen²

¹*Department of Astronomy, Columbia University, 550 West 120th Street, New York, NY 10027*

²*Center for Cosmology and Particle Physics, Physics Department, New York University, New York, NY 10003*

19 November 2018

ABSTRACT

Finding electromagnetic (EM) counterparts of future gravitational wave (GW) sources would bring rich scientific benefits. A promising possibility, in the case of the coalescence of a super-massive black hole binary (SMBHB), is that prompt emission from merger-induced disturbances in a supersonic circumbinary disk may be detectable. We follow the post-merger evolution of a thin, zero-viscosity circumbinary gas disk with two-dimensional simulations, using the hydrodynamic code FLASH. We analyze perturbations arising from the 530 km s^{-1} recoil of a $10^6 M_{\odot}$ binary, oriented in the plane of the disk, assuming either an adiabatic or a pseudo-isothermal equation of state for the gas. We find that a single-armed spiral shock wave forms and propagates outward, sweeping up $\sim 20\%$ of the mass of the disk. The morphology and evolution of the perturbations agrees well with those of caustics predicted to occur in a collisionless disk. Assuming that the disk radiates nearly instantaneously to maintain a constant temperature, we estimate the amount of dissipation and corresponding post-merger light-curve. The luminosity rises steadily on the time-scale of months, and reaches few $\times 10^{43}$ erg/s, corresponding to $\approx 10\%$ of the Eddington luminosity of the central SMBHB. We also analyze the case in which gravitational wave emission results in a 5% mass loss in the merger remnant. The mass-loss reduces the shock overdensities and the overall luminosity of the disk by $\approx 15 - 20\%$, without any other major effects on the spiral shock pattern.

Key words: black hole physics – galaxies: nuclei – gravitational waves

1 INTRODUCTION

The gravitational waves (GWs) produced during the late stages of the merger between super-massive black holes (SMBHs), with masses of $\sim (10^4 - 10^7) M_{\odot} / (1 + z)$, out to redshifts beyond $z \approx 10$, are expected to be detectable in the next decade by the *Laser Interferometric Space Antenna* (*LISA*) satellite. While the GW signatures themselves will be a rich source of information, identifying the electromagnetic (EM) counterpart of the *LISA* source would open up a whole new range of scientific opportunities, from black hole astrophysics to fundamental aspects of gravitational physics and cosmology (Kocsis et al. 2007; Haiman et al. 2009a; Phinney 2009; Bloom et al. 2009).

Whether the EM counterparts of the SMBHBs detected by *LISA* can be uniquely identified depends on the accuracy of localization by *LISA*, and on the nature of the EM emission. For the typical SMBHB detected by *LISA* at $z \approx 1 - 2$, the sky position and the redshift will be known to the accuracy of $\delta(\Delta\Omega) \sim \text{few} \times 0.1$ square degrees, and $\delta z \approx \text{few} \times 0.01$, respectively (the latter limited by weak lensing errors; e.g. Holz & Hughes 2005; Kocsis et al. 2006). Within this

three-dimensional error volume, there will be of order ~ 100 candidate galaxies, at the optical magnitude limit expected to host such SMBHBs (Kocsis et al. 2008). If the coalescing SMBHBs themselves produce bright emission comparable to luminous quasars, or are associated with some other, similarly rare subset comprising $\lesssim 1\%$ of all galaxies (such as ultra-luminous infrared galaxies), then a unique counterpart may be identified among these candidates (Kocsis et al. 2006). However, having a prediction for the spectrum and the light-curve of a coalescing SMBHB – and therefore knowing what characteristic signatures to look for – would make such identifications both more likely and more reliable.

A promising possibility is that the coalescing SMBHB produces a *variable or transient* EM signal, which can be uncovered by suitably designed EM observations, either concurrently with or following the *LISA* detection (Kocsis et al. 2008; Lang & Hughes 2008; Haiman et al. 2009a). The dense nuclear gas around the BH binary is expected to cool rapidly, and settle into a rotationally supported, thin circumbinary disk (e.g. Barnes 2002; Escala et al. 2005). The evolution of a SMBHB embedded in such a disk has been studied in

various idealized configurations (e.g. Armitage & Natarajan 2002; Liu, Wu & Cao 2003; Milosavljević & Phinney 2005; Dotti et al. 2006; MacFadyen & Milosavljević 2008; Hayasaki 2009; Cuadra et al. 2009; Haiman et al. 2009b). Generically, at small orbital separations when the binary is detectable by *LISA*, the orbit decays rapidly due to GW emission. If the disk is thin, the binary torques create a central cavity, nearly devoid of gas, within a region about twice the orbital separation (e.g. Artymowicz & Lubow 1994). Whether the decaying SMBHBs produce bright emission during this stage is not well understood. If the central cavity were truly empty, no gas would reach the SMBHBs, and any emission produced farther out in the disk would likely be weak. On the other hand, numerical simulations suggest residual gas inflow into the cavity (Artymowicz & Lubow 1996; MacFadyen & Milosavljević 2008; Hayasaki et al. 2007, 2008; Cuadra et al. 2009), which may plausibly accrete onto the BHs, producing non-negligible EM emission.

A different possibility, and the focus of the present paper, is that variable EM signatures are produced in the gas disk *promptly after* the coalescence of the SMBHB. The burst of GWs emitted during the last stages of the coalescence results in a corresponding, nearly instantaneous reduction in the binary’s rest mass. Furthermore, when compact objects coalesce asymmetrically, the linear momentum carried away by the GWs imparts a “kick” to the center of mass of the system (Bekenstein 1973; Fitchett 1983). Recent break-through in numerical relativity has allowed accurate calculations of these effects, showing that the mass loss is typically several percent (e.g. Tichy & Marronetti 2008, and references therein), while kick velocities are typically several hundred km s^{-1} , but can be as high as $4,000 \text{ km s}^{-1}$ (Baker et al. 2006, 2007, 2008; Campanelli et al. 2007a,b; González et al. 2007a,b; Herrman et al. 2007a,b,c; Koppitz et al. 2007). The circumbinary gas will respond promptly (on the local orbital timescale) to such dynamical disturbances. Importantly, the gaseous disk outside the inner cavity is expected to cool efficiently and become geometrically thin, implying that the orbital motion of the gas is supersonic. This gas is therefore susceptible to prompt shocks, which could, in principle, produce a detectable transient EM signature (Milosavljević & Phinney 2005).

Lippai et al. (2008) considered the motion of collisionless test particles in such a disturbed disk. As long as the particles remain bound to the central SMBHB, they follow elliptical Kepler orbits (in the inertial frame of the SMBHB). These orbits cross, and produce a characteristic, outward-propagating spiral caustic. While these results were obtained in a pressureless “dark matter” disk, they suggest that shocks, with a similar pattern, will indeed arise in the gas, on times-scales of \sim weeks to \sim months after the coalescence. Similar conclusions were reached by Shields & Bonning (2008) and by Schnittman & Krolik (2008), using N-body simulations and semi-analytical arguments, respectively, to show that a bright, post-merger “flare” may occur. Both of these studies focused on the evolution of disks around more massive BHs on longer ($\sim 10^4 \text{ yr}$) time-scales, and proposed detecting the flare by monitoring a population of active galactic nuclei (AGN). By comparison, our analysis here focuses on the disks around lower-mass BHs and on the shorter time-scales of several weeks to a year, which

are relevant for follow-up observations triggered by *LISA* detections.

Motivated by the above, in the present paper, we follow up on earlier work, and compute the response of the gas disk including the effects of gas pressure using hydrodynamical simulations. Our main goals are (i) to assess shock formation in hydrodynamical disks, and (ii) to estimate the amount of dissipation and the resulting light-curve produced by the disk. In particular, for the latter, we will use simulations with a pseudo-isothermal equation of state. This corresponds implicitly to strong dissipation, and should represent an approximate upper limit on the disk luminosity. Our computations are performed with the publicly available code FLASH (Fryxell et al. 2000).

Two other, independent studies have recently used 3-dimensional simulations to address the response of gas disks to mass-loss (O’Neill et al. 2009) and to both mass-loss and kicks (Megevand et al. 2009). The main difference between our analysis and these previous works is our inclusion of runs with a pseudo-isothermal equation of state, which modifies, qualitatively, the expected EM signature. In particular, O’Neill et al. (2009) and Megevand et al. (2009) both run simulations with an adiabatic equation of state, and find that in most cases, the gas disk typically *dims* following the merger. We observe a similar effect in our adiabatic runs, and attribute it to an overall dilution of the gas density. However, the gas develops significantly larger density contrasts in our pseudo-isothermal runs, and we argue that this can result in a significant *brightening* of the system. Another important difference between our study and those of O’Neill et al. (2009) and Megevand et al. (2009) is that we perform two-dimensional simulations, whereas O’Neill et al. (2009) and Megevand et al. (2009) both utilized 3D simulations. While we have sacrificed resolving the vertical disk structure, this allows us to simulate a disk that extends to much larger radii (10^4 Schwarzschild radii), and follow the entire disk for a much longer period ($\sim 1 \text{ yr}$ for a $10^6 M_{\odot}$ binary), in order to cover the regime relevant for follow-up observations of *LISA* events. Given the expected size of the inner cavity in the disk, $\sim 100 R_s$, studying these outer regions of the disk, and following the disk evolution on the correspondingly longer time-scale, is especially important. Further differences between our study and those of O’Neill et al. (2009) and Megevand et al. (2009) will be discussed in § 3.6 below.

The rest of this paper is organized as follows. In § 2, we describe our computational setup, including details of the simulations, and initial conditions. In § 3, we present and discuss our main results. These include the impact of the kick (§ 3.1) and the mass-loss (as well as both effects in combination; § 3.2), using constant surface density disks. In § 3.3, we discuss our estimate of the post-merger light curves. In § 3.4, we repeat our calculations at higher resolution and with more realistic initial gas density and temperature profiles (adapted from a standard α -disk). In § 3.5, we discuss possible numerical issues, and in § 3.6, we compare our results to previous work. Finally, in § 4, we summarize our main conclusions and their implications, and outline natural future extensions of this study.

2 INITIAL CONDITIONS AND SIMULATION DETAILS

Our calculations were performed with version 2.5 of the publicly available Advanced Simulation and Computing (ASC) Flash code, developed at the University of Chicago. This code uses the split piece-wise parabolic method (PPM), making it well-suited for modeling shocks (Fryxell et al. 2000). We use a uniform-mesh grid in polar coordinates to simulate a two-dimensional vertically averaged disk. Our runs cover a physical duration much shorter than the viscous time-scale, and we therefore do not include any physical viscosity. The central black hole is chosen have a mass of $M = 10^6 M_\odot$, which is approximately the most favorable value for detection by *LISA* (although our results can be re-scaled to apply to BHs with different masses; see § 3.5). The inner edge of the grid is located $100R_s$ (Schwarzschild radii), the radius at which the central gap opened by a binary black hole is expected to freeze (Milosavljevic & Phinney 2005; Haiman et al. 2009b).

A high-resolution mesh is used for radii between $100 < R/R_s < 10^4$ for all simulations, except the runs *Kad1-5* (see Table 1 below), which use a high-resolution mesh between $100 < R/R_s < 1.5 \times 10^4$. A lower-resolution mesh extends to $3.1 \times 10^5 R_s$. We tested the effect of boundary conditions by simulating a disk in Keplerian motion without the influence of mass loss or kick. Within the 486 days we simulate after the merger, numerical fluctuations contributing to the density and luminosity of the disk were confined within the $100 < R/R_s < 10^3$ region. The amplitude of the numerical density perturbations was well below the over-densities produced by shocks in the disturbed disks, so in our analysis of the densities and morphologies of the shocks, we include the entire high-resolution mesh region, down to $100R_s$. However, the contribution of this low-amplitude noise to the luminosity was still significant. As a consequence, our post-processing analysis related to the disk luminosity is restricted to radii between $10^3 < R/R_s < 10^4$; corresponding to 30 days $\lesssim t \lesssim 1$ year (see discussion of this issue in § 3.5 below).

In our fiducial run (see “*Kiso3*” in Table 1 below), the high-resolution grid contains zones with sizes $\Delta r = 20R_s$ and $\Delta\theta = 0.01$ radians, which is the effective spatial resolution of this run. This run had a corresponding numerical time-resolution, in physical units, of $\Delta t \approx 35$ seconds. However, to save disk space, FLASH outputs were made only at every $\approx 10^4$ th time-step, allowing us to sample the results on time-scales of ≈ 4 days. In physical units, the total simulated time interval is 486 days (or $\sim 1.4 \times 10^7 M$, in gravitational units with $G = c = 1$). For comparison, the orbital time at the inner and outer edge of our disk is ~ 4 hours and 0.5 years, respectively, so that our simulations cover approximately 3000 and 3 full orbits at these radii. To test the numerical convergence of our results, we performed three additional variants of the fiducial run, one at lower resolution, with $(\Delta r, \Delta\theta) = (40 R_s, 0.02 \text{ rad})$, and two at higher resolutions of $(\Delta r, \Delta\theta) = (10R_s, 0.005 \text{ rad})$, and $(\Delta r, \Delta\theta) = (5 R_s, 0.0025 \text{ rad})$. The corresponding physical time-steps in these runs were $\Delta t = 70, 17.5$, and 8.75 seconds, respectively.

It has been shown that the black hole binary can excite eccentricities in the disk within a region comparable

to the binary separation (MacFadyen & Milosavljević 2008; Hayasaki et al. 2007, 2008; Cuadra et al. 2009). This region shrinks as the binary separation shrinks, and our region of interest ($> 10^3 R_s$) is an order of magnitude larger than the binary separation when gravitational radiation first dominates the inspiral timescale. We therefore assume that the gas orbits have had time to circularize, and initially follow zero-eccentricity Kepler orbits.

The disk is assumed to consist of ideal gas, and for simplicity, we use the constant gamma-law equation of state employed by FLASH. We chose the value $\gamma = 5/3$, corresponding to monatomic ideal gas. However, the equation of state can be calculated using one of two methods. The first method is used in simulations we call “adiabatic,” which use the internal energy of each mesh zone to calculate the temperature and pressure for the respective zone. The second method is “isothermal” for which temperature is used to calculate the internal energy and pressure for each zone. The temperature used in these calculations is held fixed throughout the disk for the duration of the simulation at a pre-specified value. In practice, this forces $P \propto \rho$, but keeps E_{int} constant. Our adiabatic and isothermal runs should be considered limiting cases, which bracket the true behavior of a thin disk with a more realistic treatment of radiative cooling.

For simplicity, in a first set of runs, we assume the disk initially has a constant surface density ($\Sigma = 1.5 \times 10^5 \text{ g cm}^{-2}$; the total mass of the disk is $2.1 \times 10^3 M_\odot$) and a constant temperature (chosen from the range $4.5 \times 10^2 \text{ K} \leq T \leq 1.4 \times 10^8 \text{ K}$). These choices are broadly motivated by the physical values expected in a standard α -disk around a $10^6 M_\odot$ black hole (e.g. Frank et al. 2002). In a second set of runs, we adopt radial power-law profiles for the surface density, temperature, and scale-height, given by

$$\Sigma(R) = 6.10 \times 10^5 \left(\frac{M}{10^6 M_\odot} \right)^{\frac{1}{5}} \left(\frac{R}{100R_s} \right)^{-\frac{27}{40}} \text{ g cm}^{-2} \quad (1)$$

$$T(R) = 5.84 \times 10^6 \left(\frac{M}{10^6 M_\odot} \right)^{-\frac{2}{10}} \left(\frac{R}{100R_s} \right)^{-\frac{33}{40}} \text{ K} \quad (2)$$

$$H(R) = 1.46 \left(\frac{M}{10^6 M_\odot} \right)^{-\frac{1}{10}} \left(\frac{R}{100R_s} \right)^{\frac{87}{80}} R_s, \quad (3)$$

The scale-height $H(R)$ is not actually used in the 2D simulation, but we use it in § 3.6 below to compute the 3D gas density, needed to predict the Bremsstrahlung luminosity. For a standard α -disk, with common choices for the viscosity parameter, disk opacity, and other parameters, the power-law slopes of the physical parameters are somewhat different in the “inner” (radiation pressure- and electron scattering opacity-dominated) and “middle” (gas pressure- and electron scattering opacity-dominated) regions. The transition between these two regimes occurs around $\sim 10^3 - 10^4 R_s$ for typical disk parameters, but the power-law slopes in these two regimes are, in any case, quite similar (see, e.g., Haiman et al. 2009b). The power-law slopes we adopt in equations (1)-(3) are averages between the values in these two disk regions. Note that the total mass of our α -disk is $580 M_\odot$, somewhat lower than the mass of our uniform disk.

The presence of the circumbinary disk is expected to align the spins of both BHs during the early stages of their evolution (at large separations), to be parallel with the an-

Table 1. Summary of constant initial surface density disk simulation runs. In all runs, the central BH has a mass of $10^6 M_\odot$, and the disk extends from 10^2 to 10^4 Schwarzschild radii. In runs that include a kick, the kick velocity is 530 km s^{-1} , oriented in the plane of the disk, and in runs that include mass loss, the fractional loss is assumed to be 5%.

Simulation Type	Adiabatic	Isothermal	Temperature
kick only (no mass loss)	Kad1	Kiso1	450 K
	Kad2	Kiso2	4500 K
	Kad3	Kiso3	1.4×10^5 K
	Kad4	Kiso4	4.5×10^5 K
	Kad5	Kiso5	1.4×10^6 K
			Kiso6
Higher-resolution version of Kiso3	–	Kiso3 ⁺	1.4×10^5 K
Highest-resolution version of Kiso3	–	Kiso3 ⁺⁺	1.4×10^5 K
Low-resolution version of Kiso3	–	Kiso3 [–]	1.4×10^5 K
mass loss only (no kick)	Mad3	Miso3	1.4×10^5 K
mass loss and kick	–	MKiso3	1.4×10^5 K

Table 2. Summary of simulation runs with an initial α -disk profile. As in the constant surface density runs, the central BH has a mass of $10^6 M_\odot$, and the disk extends from 10^2 to 10^4 Schwarzschild radii; the kick velocity is 530 km s^{-1} , oriented in the plane of the disk, and the fractional mass loss is 5%. The resolution in all α -disk runs is the same as in the highest-resolution constant-density run Kiso3⁺⁺.

	Simulation Type	Abbreviation
Isothermal	kick only (no mass loss)	Kiso
	mass loss only (no kick)	Miso
	kick and mass loss	MKiso
Adiabatic	mass loss only (no kick)	Mad
	kick and mass loss	MKad

gular momentum of the disk (Bogdanović et al. 2007). In this case, the recoil will be oriented within the plane of the disk; in any case, the two-dimensional nature of our simulations precludes us from studying out-of-the-plane kicks. We further use the typical value of 530 km s^{-1} (Baker et al. 2008) throughout this paper. Our simulations are set up in the reference frame traveling with the kicked SMBHB. Since the total disk mass within our simulated region of $100 - 10,000 R_s$ is only a fraction $\sim 10^{-3}$ of the SMBHB mass, we neglect the inertia of the gas bound to the SMBHB. In practice, we simply add a unidirectional velocity component to the gas, everywhere in the plane of the disk, in our initial conditions, on top of the circular Kepler velocities. In runs which include a mass loss, we adopt a fractional loss of 5% – i.e., the disk is set up as before, but the central mass is reduced to $9.5 \times 10^5 M_\odot$ at the first time-step of the simulation.

Tables 1 and 2 summarize the parameters of all of our

simulations. The runs were performed at the Center for Cosmology and Particle Physics at New York University using the Ria cluster. Ria has 368 2.6 GHz CPUs with Infiniband interconnect and 768 GB of memory. For reference, we note that our fiducial run, labeled *Kiso3*, was run on three nodes (24 processors), and took four days to complete.

3 RESULTS AND DISCUSSION

3.1 Post-Merger Disk Evolution and Shock Structure

Figure 1 shows snapshots of the two-dimensional surface density distribution in our fiducial isothermal (*Kiso3*; left panel) and adiabatic (*Kad3*; right panel) simulations $t = 210$ days after the merger. As the figure shows, sharp overdensities develop in both cases, with a morphology similar to the spiral caustics in the collisionless case (Lippai et al. 2008). The density contrasts are visibly higher in the isothermal case, as one intuitively expects from the higher compressibility of isothermal gas.

The sharpness of the thin arcs traced out by the overdense regions suggest the presence of shocks. To assess whether shocks have indeed formed, once the simulation runs have completed, the output files were tested with an algorithm identical to the *shock.detect* feature available in FLASH. To receive a shock flag, a zone must pass both of the following criteria. First, the pressure difference between the zone and at least one of its neighbors must exceed the difference expected from the Rankine-Hugoniot jump conditions for a shock of a pre-specified minimum Mach number \mathcal{M} . To allow for oblique shocks, while comparing each zone to its neighbors in different directions, the pressure is weighted according to the fraction of the total velocity made up by the velocity vector in the appropriate direction. Second, to avoid falsely flagging expanding regions as shocks, the velocity divergence at the zone in question must be negative.

The zones identified by the above criteria shows that shocks indeed arise in our runs at early times, and propagate outward. Shocks at early times in the disk were found to be typically weak. For example, in our *Kiso3* run, at $t = 30$ days, among the shocked zones identified with the threshold $\mathcal{M} > 1.1$, we find that 20% exceeded $\mathcal{M} > 2$. Subsequently, the shocks increased in strength, as they moved outward (with the top 20% of the shocked zones having $\mathcal{M} > 3$ by $t = 200$ days). Shocks appeared in all of our runs except *Kiso6* – in this run, the constant isothermal temperature was increased to correspond to a sound speed of $c_s \approx 10^3 \text{ km s}^{-1}$, approximately two times larger than v_{kick} . This suggests that $v_{\text{kick}} \gtrsim c_s$ can be used as an approximate criterion for the kick to cause shocks. This is consistent with the expectation in collisionless disk, in which particles cross their epicyclic orbits with a relative velocity of $\Delta v \sim v_{\text{kick}}^2/v_{\text{orbit}}$; in bound regions of the disk, this relative velocity is limited to $\Delta v \lesssim v_{\text{kick}}$ (Lippai et al. 2008).

In Figure 2, we show the radial position of the densest point identified at several different times in the isothermal (*Kiso1-6*; upper panel) and adiabatic (*Kad1-5*; lower panel) runs, together with the surface density enhancement at this point, defined as $\Delta\Sigma \equiv \Sigma/\Sigma_i$ (where Σ_i is the initial constant surface density). The points are shown every 4 days,

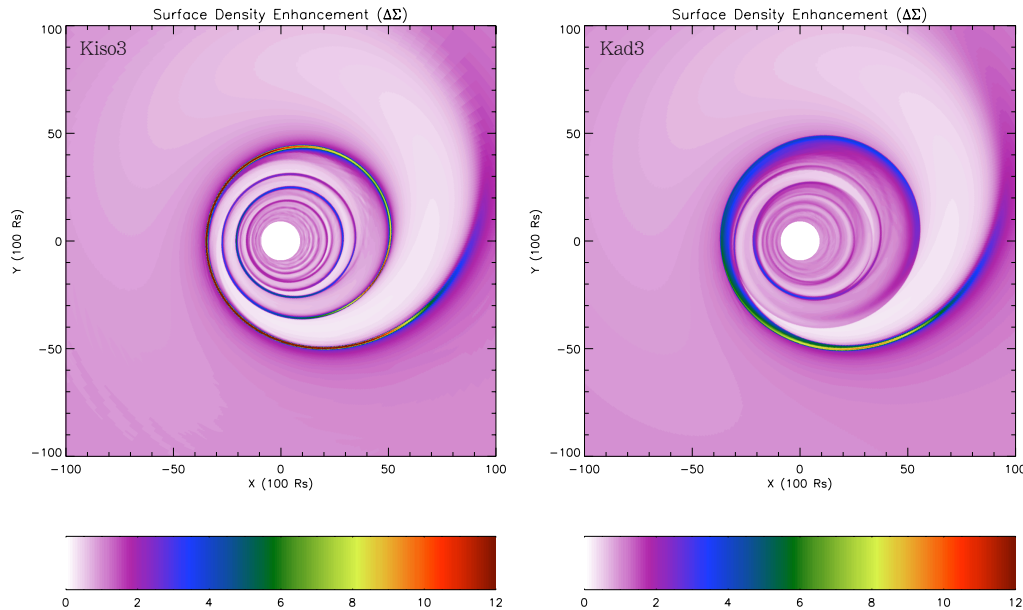


Figure 1. Contour images of the surface density distributions in our fiducial isothermal (*Kiso3*; left) and adiabatic (*Kad3*; right) simulations at $t = 210$ days following the merger and the recoil of the SMBHB. In both cases, the rotation of the disk is clockwise, and the direction of the kick is up along the y axis; the disks are shown in Cartesian coordinates extending to $10^4 R_s$. The color scales at the bottom are in units of the overdensity, relative to the constant initial surface density.

between $t = 4$ and $t = 300$ days after the merger, with 4 days corresponding to the left-most point, and 300 days to the right-most point. In the isothermal runs the densest point in the shock wave tends to stay at the same azimuthal position in the disk, $\sim 3\pi/2$ rad (as measured clockwise from the y axis), which corresponds to the region of the disk where the kick direction is parallel to the tangential velocity of gas in the disk. The kick adds constructively to the Keplerian velocity of gas at the angle $3\pi/2$, and it is not surprising that gas at this azimuthal position achieves the largest over-densities first.

In Figure 3, we show the radial position of the densest point in the disk as a function of time, in the same 10 runs as in Figure 2 (*Kiso6* is excluded). For comparison, the black squares show the location of the outermost caustic identified in a collisionless case (Lippai et al. 2008; see further discussion in § 3.6 below). The location of the isothermal shocks follow the caustics quite closely. However, interestingly, after $t \approx 100$ days, the densest shock appears to propagate \sim twice as rapidly in the adiabatic simulations. As Figure 1 shows, the overall size and morphology of the sharp spiral patterns forming in the isothermal and adiabatic runs are quite similar, except that in the adiabatic runs, the spiral arms are more diffuse and each arm tends to extend to a somewhat larger radius than in the corresponding isothermal case. The difference in the apparent radial propagation speed of the densest point arises because typically, in the adiabatic runs (i) the densest point falls further out along the outermost spiral arm, and (ii) the outermost spiral arm extends to slightly a larger radius. Furthermore, the densest point is typically farther out along the spiral pattern in adiabatic disks with increasing temperatures. Interestingly, the adiabatic run with the hottest temperature (*Kad5*) is an exception; in this run, the densest point again falls further

in along the outermost spiral arm, which is noticeably more diffuse compared to the *Kad4* run. The spiral arms in the adiabatic runs also tended to diffuse over time, with pairs of adjacent arms eventually overlapping. In comparison, the isothermal spiral arms remained distinct and did not interact. This likely explains why the isothermal curves are much smoother than the adiabatic curves.

These figures also illustrate the strength of the density perturbations caused by the kick, allowing us to draw several interesting conclusions. In particular, as the temperature, and therefore the pressure increases, the density enhancements generally decrease, as expected. The two lowest temperature cases ($T = 450$ and $4500K$) differ very little in either the adiabatic or isothermal case, indicating that pressure effects are negligible when the disk temperature is below $T \approx 4500K$. Also as expected, the overdensities are much larger in the isothermal runs, reaching $\Delta\Sigma \gtrsim 40$ in our fiducial *Kiso3* case, and still rising at the end of the run, whereas in the adiabatic run with the same temperature (*Kad3*), the overdensity reaches a plateau and is limited to $\Delta\Sigma < 10$. Pressure has little effect at very early times (except for the extremely hot disk *Kiso6*), when the shocks are within $\lesssim 10^3 R_s$ and have relatively low-overdensities. Note that the sound crossing time near the inner edge of the disk in our fiducial run is $R/c_s \approx 70$ days, comparable to the time when pressure starts to have an impact on the shock overdensities. Interestingly, pressure suppresses density enhancements at late times by large factors. This last conclusion is somewhat surprising, given expectations from collisionless disks (see further discussion of this point in § 3.6 below).

In Figure 4, we show the total mass of the shocked material divided by the total mass of the disk at a given time, all within the high-resolution mesh region ($100 < R/R_s < 10^4$

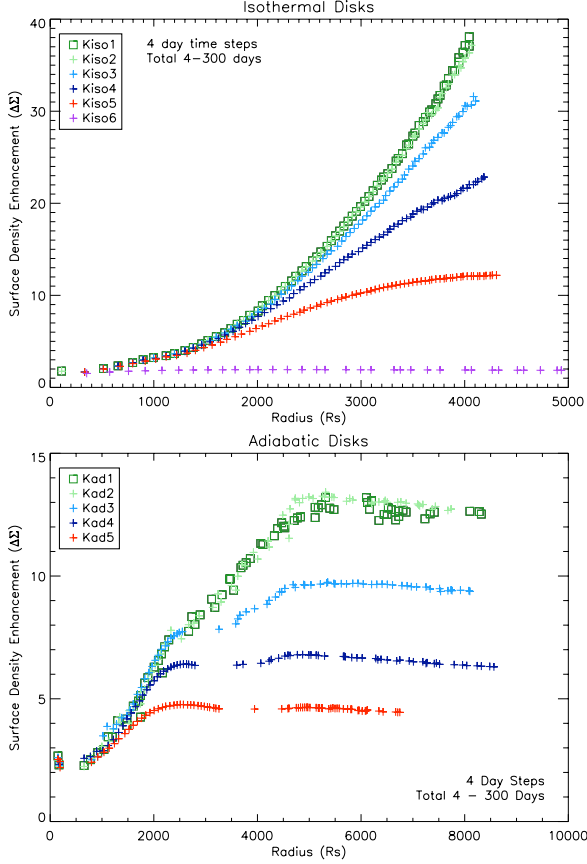


Figure 2. Evolution of the maximum surface density in our isothermal (*Kiso1-6*; upper panel) and adiabatic (*Kad1-5*; lower panel) runs. The points show the radial position and the local overdensity at the densest point in the disk, identified at several different times between $t = 4$ and $t = 300$ days after the merger (with 4 days corresponding to the left-most point, and 300 days to the right-most point).

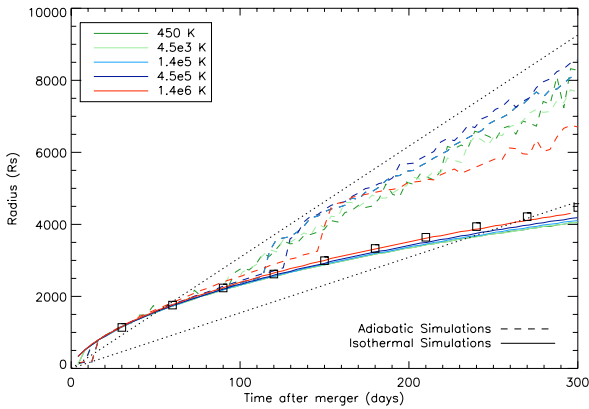


Figure 3. The figure shows the radial location of the densest point in the disk as a function of time. The same runs are shown as in Figure 2, with the same notation (except *Kiso6* is excluded, since it had no shocks). For comparison, the black squares show the location of the outermost caustic identified in a collisionless disk (Lippai et al. 2008). The straight dotted lines correspond to propagation at constant speeds of $v_{\text{kick}} = 530 \text{ km s}^{-1}$ (lower line) and $2v_{\text{kick}} = 1060 \text{ km s}^{-1}$ (upper line).

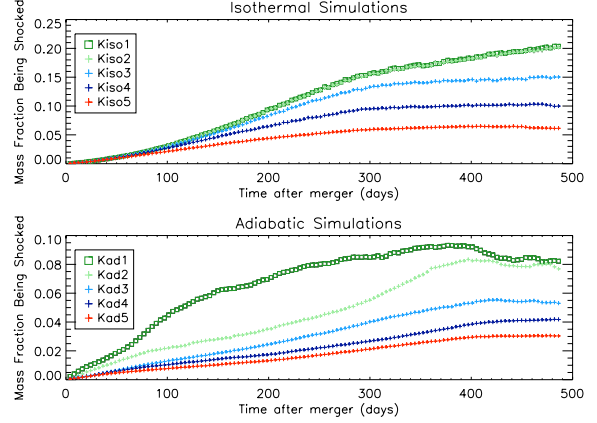


Figure 4. Mass fraction of the disk material undergoing a shock with a minimum Mach number of $\mathcal{M} \geq 1.1$, as a function of time. The different symbols correspond to the runs shown in Figure 2. The curves begin to flatten when the outermost part of the spiral pattern begins to leave the high-resolution mesh region, in both the isothermal (~ 250 days) and the adiabatic simulations (~ 400 days; note that in the adiabatic runs, a larger mesh was used, extending to $15,000R_s$).

for *Kiso1-5*, and $100 < R/R_s < 1.5 \times 10^4$ for *Kad1-5*) using the shock criteria defined above, and a minimum Mach number of $\mathcal{M} = 1.1$. For cold isothermal disks, a significant fraction of the disk ($\sim 20\%$) can be experiencing a shock at a given moment. The shocks in the adiabatic cases comprise a smaller fraction of the disk, because the temperature and pressure ($\propto \rho T$) both increase in the compressed regions, reducing the bulk velocities and shock strengths. Overall, compared to the isothermal cases, in the adiabatic runs the density enhancements are reduced, and shocks are weakened and are less prevalent – these trends are as expected, and follow from the lower compressibility of adiabatic gas.

3.2 Impact of Mass-Loss

The results in the previous section included only the effect of the kicks, and not the effects of the accompanying mass loss. Upon coalescence of the SMBH binary, energy is carried away by gravitational waves, causing an instantaneous reduction of the rest mass by the amount of $(M_1 + M_2)\epsilon_{GW}$. The fractional loss depends on the mass ratio, on the orbital parameters, and on the magnitude and orientation of both BH spins, for which the full parameter space has not yet been explored in direct relativistic numerical simulations. For nearly equal mass binaries ($q \equiv M_1/M_2 \sim 1$), however, the mass loss can be several percent (e.g. Tichy & Marronetti 2008; Herrman et al. 2007a). For simplicity, throughout this paper, we adopt a constant fractional mass loss of 5%. We initialize the disk with Keplerian velocities for the original pre-merger point mass $(M_1 + M_2) = 10^6 M_\odot$. However, in the remainder of the simulation, the gravitational potential is that of a central point mass with $(M_1 + M_2)(1 - \epsilon_{GW}) = 9.5 \times 10^5 M_\odot$.

The effects of such an instant mass-loss was treated recently by O’Neill et al. (2009) and Megevand et al. (2009) in three-dimensional adiabatic disks. Here we extend these works by following the impact of the mass-loss case in an

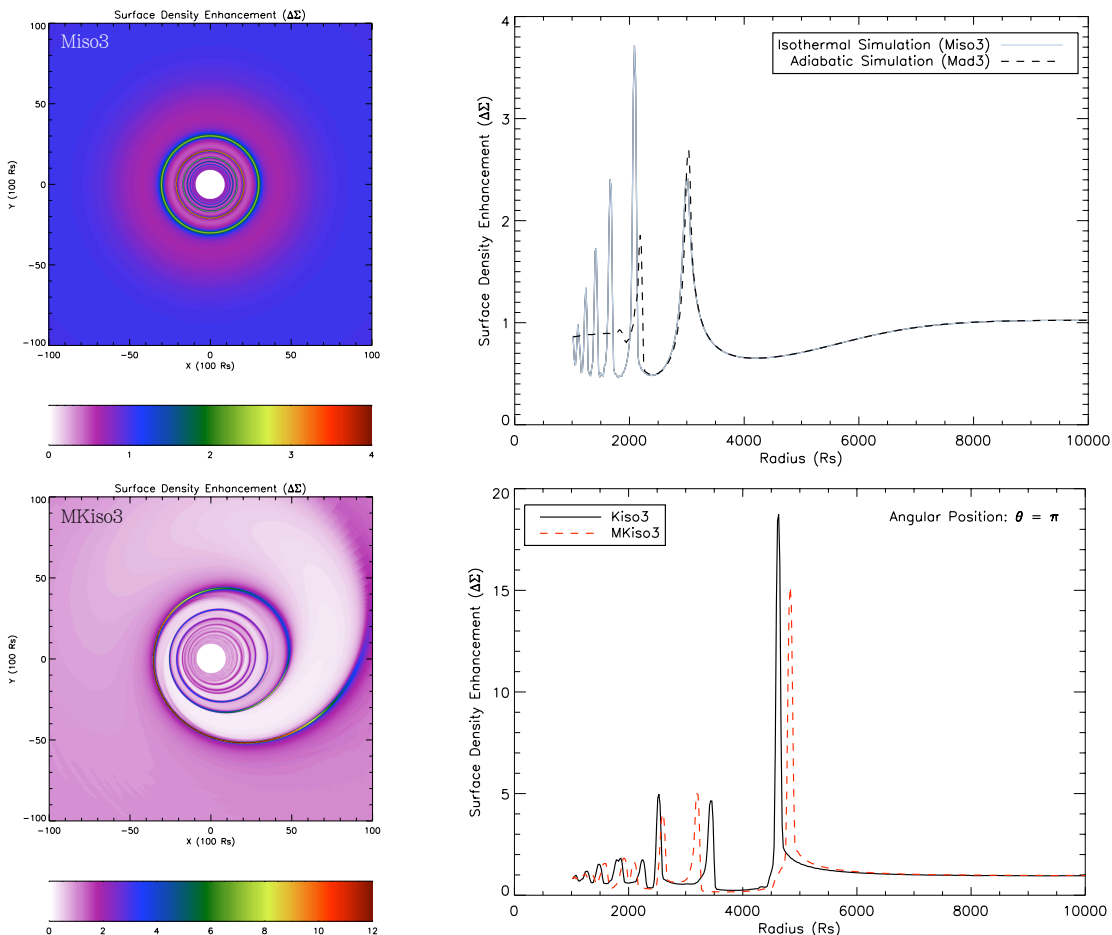


Figure 5. *Top panel:* The left-hand side contour map shows the surface density for an isothermal 1.4×10^5 K disk, where the central BH experiences sudden mass-loss by 5% (*Miso3*). No kick is included. Concentric rings of density spikes develop and propagate outward, here shown at $t = 210$ days after the merger. The figure on the right shows the radial profile of the disk surface density for the isothermal disk (*Miso3*) in comparison to surface density from the adiabatic disk (*Mad3*) which was subjected to the same initial setup. *Bottom panel:* The contour map on the left shows the surface density of a disk at $t = 210$ days after the merger. A kick, with $v_{\text{kick}} = 530 \text{ km s}^{-1}$ is included in addition to the mass loss (*MKiso3*). In the right panel, we also show, for comparison, the radial overdensity profile in our isothermal disk that includes only a kick, and no mass loss (*Kiso3*). Interestingly, the addition of the mass-loss results in a small reduction of the kick-induced overdensities (as well as a slightly faster outward-propagation of the outermost shock).

adiabatic (*Mad3*) as well as in an isothermal disk (*Miso3*). In the latter case, we also investigate the combined impact of mass loss and recoil (*MKiso3*). As noted in the Introduction, having one less dimension allows our simulations to cover the disk out to a much larger radius ($10^2 - 10^4 R_s$ vs. the range $2 - 50 R_s$ in O’Neill et al. 2009), and for a much longer duration ($\sim 1 \text{ yr}$ vs. $\sim 5 \text{ hrs}$ in O’Neill et al. 2009; for a $10^6 M_\odot$ BH).

The top portion of Figure 5 shows a surface density map of an isothermal disk, in the mass-loss case, around $t = 210$ days after the merger (in the left panel). In the right panel of the same figure, we show the radial surface density profile of the same disk, together with the profile of an adiabatic disk with the same mass-loss. When the impact of the kick is not included, the perturbations are azimuthally symmetric, giving rise to concentric, outward-propagating ripples. The basic mechanism behind creating the ripples can be visualized simply as follows: at the moment of mass loss, each particle, orbiting at its original Keplerian velocity, is moving at a speed that is too fast for a circular orbit around the re-

duced central mass. As a result, all particles find themselves at the pericenter of a new, elliptical orbit. Summing the effective contributions of each particle to the surface density, spread over these orbits, results in a net *dilution* of the disk. Furthermore, the radial epicyclic oscillations of the set of particles at a fixed initial radius will occur at a frequency that monotonically decreases radially outward, resulting in a pattern of quasi-periodic compression / decompression in the radial direction. The resulting density spikes have lower amplitudes, but are more frequent toward the inner boundary. These effects are clearly seen in Figure 5 except that, notably, the pressure forces in the adiabatic case are sufficient to almost completely wash out the innermost density ripples, out to $R \lesssim 2,000 R_s$, by $t = 210$ days.

When a kick is included in addition to the mass-loss (*MKiso3*), the density enhancements are often lower in comparison to the kick-only case (*Kiso3*). The bottom portion of Figure 5 shows a map of the surface density and a radial slice of the surface density profile along the azimuth $\theta = \pi$ (running in the direction of the $-y$ axis) in both cases. The

density enhancement from the mass-loss + kick run is appreciably lower than in the kick-only case, especially for the outermost, densest spike, at $R \approx 4,500 - 5,000R_s$.

3.3 Observational Signatures

Our adiabatic runs conserve energy, so, by definition, no energy loss occurs in these runs, and the disk has strictly zero luminosity. In reality, the disk will radiate – indeed, a prediction of its time-variable light-curve, following the merger, will be invaluable for identifying EM counterparts to *LISA* sources. A realistic prediction requires solving for the vertical structure of the disk, as well as a treatment of radiative cooling and radiative transfer across the disk (which is likely to be optically thick; see below). While this is not possible in our 2D simulations, our isothermal runs allow us to calculate the energy dissipation occurring in the disk – this can serve as a rough, order-of-magnitude estimate for the disk luminosity.

More specifically, at each time-step, FLASH solves Euler’s equations, expressed in conservation form, to update the total specific energy (E) of each zone which includes the combined kinetic and internal energy. In our case, the disk is cold, and the internal energy (E_{int}) is very small compared to the kinetic energy of orbital motion, and is therefore a small fraction of the total energy E . This can cause numerical inaccuracies, and we found that it was necessary to solve for E_{int} explicitly, using an internal energy advection equation that is separate from the total energy¹. The pressure (and temperature, if required) of the zone is subsequently obtained using the specified equation of state.

When an isothermal equation of state is used, the pre-specified constant initial temperature T^{iso} is used to calculate the internal energy, so that it is reset to $E_{\text{int}}^{\text{iso}} = (\gamma - 1)^{-1} \rho k T^{\text{iso}} / \mu m_p \propto \rho$. The difference of the internal energies before and after this re-set, $\Delta E_{\text{int}} = E_{\text{int}} - E_{\text{int}}^{\text{iso}}$, corresponding to the $p\Delta V$ work done by the gas, is effectively radiated instantaneously; we compute the corresponding luminosity by dividing ΔE_{int} by the simulation time-step.

The light curve obtained by this method corresponds to the limiting case of efficient radiative cooling that keeps the gas at constant temperature. An ambiguity in this interpretation arises, however, in zones which expand, and therefore would cool, in the adiabatic case. The isothermal condition requires that these fluid elements gain, rather than lose energy, in order to maintain their constant temperature. The above calculation simply returns a negative luminosity in these zones, which should either be excluded from the total luminosity budget (if, in reality, these zones remain cooler than T^{iso}), or may be included (under the assumption that the corresponding heating comes at the expense of the radiation generated in the compressed regions). Clearly, the isothermal approach is not adequate by itself to resolve this ambiguity, and below we will simply quote luminosities both with and without the negative contribution of these expanding zones. These may also be regarded as upper and lower limits; our light-curves are inherently limited to an accuracy

¹ See equation 13.7 in the FLASH User Guide, Version 3.2, July 2009; available at http://flash.uchicago.edu/website/codesupport/flash3_ug_3p2.pdf.

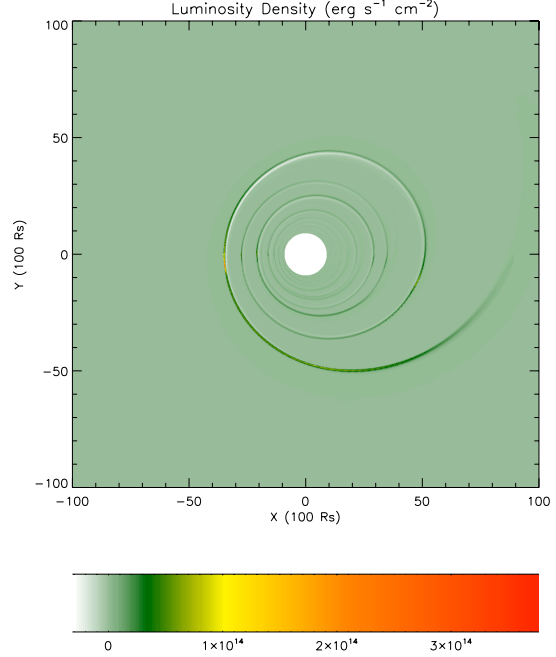


Figure 6. A snapshot of the luminosity density, defined as the energy radiated per unit area and unit time, in our fiducial *Kiso3* run, here shown at $t = 210$ days. The bright regions, with a high positive luminosity, closely trace the spiral shocks seen in Figure 1. The color scale shown at the bottom of the figure is in units of $\text{erg s}^{-1} \text{cm}^{-2}$. Note the negative contributions from the post-shock regions (see text for discussion).

comparable to the difference between these two estimates (which we find is typically a factor of \sim two).

Figure 6 shows a snapshot of the luminosity density, defined as the energy radiated per unit area in a single time-step Δt , $j \equiv \Delta E_{\text{int}} / \Delta A \Delta t$ in our fiducial *Kiso3* run, at $t = 210$ days. As noted above, the luminosity in the region inside $R < 10^3 R_s$ is dominated by numerical noise. To be conservative, we have therefore excised these inner regions from our luminosity calculations. Outside $R < 10^3 R_s$, the bright regions, with a high positive luminosity, clearly trace the shocks quite well, which is indeed what one expects, since these are the locations where the gas is being most compressed. Adjacent to the bright shocks, the figure also shows regions of post-shock decompression, where the velocity divergence is positive, and the luminosity is negative.

In Figure 7, we show the corresponding light curves in our fiducial run (*Kiso3*) – again, conservatively, limited to the region $10^3 < R/R_s < 10^4$ – when only the positive-luminosity zones are considered (black solid curve) and when the contribution from the negative-luminosity zones is subtracted (black dotted curve). The other curves in this figure show how the light-curves depend on numerical resolution, and will be discussed in § 3.5 below. The absolute value of the luminosity is significant, corresponding to $\approx 16\%$ of the Eddington luminosity L_{Edd} for a $10^6 M_\odot$ black hole in the first case, and reduced by less than a factor of two, to $\approx 10\% L_{\text{Edd}}$ in the latter case. We note that despite the significant luminosity, the total energy radiated in the first year after the merger (integrating the light curve in Figure 7) is found to be $\approx 0.1 \times M_{\text{disk}} v_{\text{kick}}^2$. In principle, the

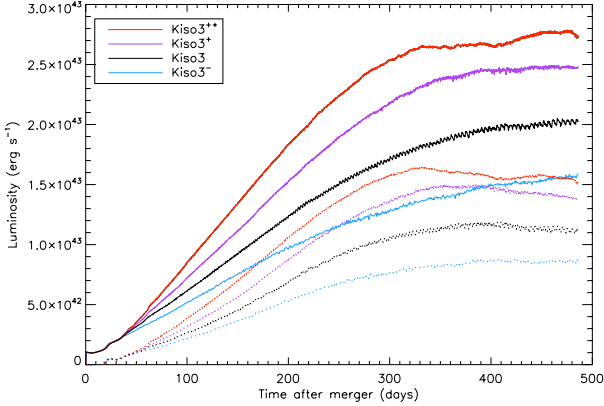


Figure 7. Light-curves obtained in $T = 1.4 \times 10^5$ K isothermal disks experiencing a kick, by integrating the luminosity density, such as shown in Fig. 6, across the surface of the disk. The solid curves include only the positive-luminosity zones, whereas the dotted curves include the contribution from the negative-luminosity zones. The black curves are derived from our fiducial run (*Kiso3*), and the magenta/red/blue curves show the results of a resolution study (corresponding to the high-resolution runs *Kiso3*⁺⁺ and *Kiso3*⁺; and the low-resolution run *Kiso3*⁻, respectively). The total positive luminosity in the highest-resolution run (top curve) reaches $\approx 20\%$ of the Eddington limit for a $10^6 M_\odot$ black hole.

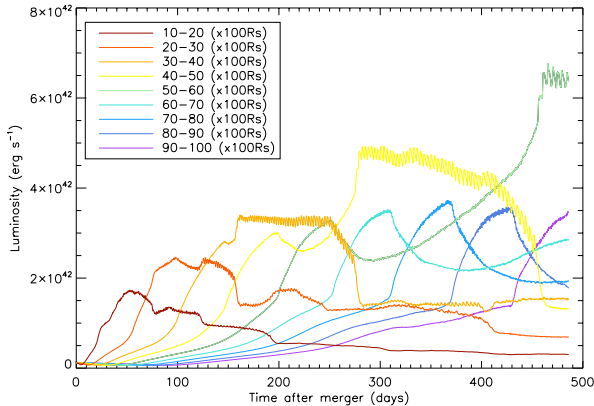


Figure 8. Contributions to the total (positive) luminosity from different annuli in the fiducial run *Kiso3*, as labeled. The densest shocked region of the disk tends to dominate the total luminosity, and each annulus provides a maximum contribution when this “bright spot” moves across it.

kick-induced dissipation could extract and radiate away a non-negligible fraction of the total potential energy of the disk; the luminosity we find implies an energy release well below this upper limit.

In Figure 8, we decompose our light-curve, and show the contribution of the positive-luminosity zones from different annuli in the disk, binned by radius. The densest shocked region of the disk tends to dominate the total luminosity, and, as the figure shows, each annulus provides a maximum contribution when the “bright spot” moves across it. The luminosity rises steadily overall, which is attributable predominantly to having more radiating material at larger radii (the bins shown in Fig. 8 have equal radial widths, so their

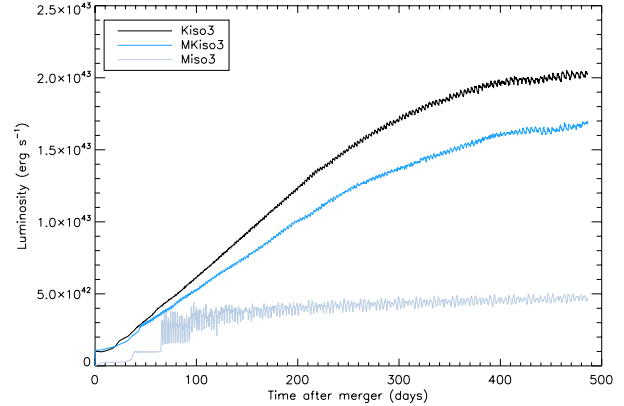


Figure 9. Light curves as in Figure 7, except here we contrast the results from the mass-loss only (*Miso3*), mass-loss + kick (*MKiso3*), and the kick-only cases (*Kiso3*). When the effect of mass-loss is included in addition to the kick, it reduces the overall luminosity of the disk by a modest factor. In the case of mass-loss only, the luminosity of the disk is reduced significantly (by a factor of ≈ 4).

area grows linearly with radius). As discussed above, the shocks also get stronger with time; however, this is a relatively weak effect, and the overall rise in the luminosity, seen in Figure 7, roughly tracks the build-up of the shocked mass (see Fig. 4). At the most luminous portion of the shock, in our fiducial run, the temperature typically rises during each time step by $\approx 4\%$, before it is re-set to 1.4×10^5 K.

When the effects of mass-loss are included in the simulation, in addition to the kick, the luminosity of the disk tends to decrease. This can be expected from Figure 5, which showed that the overdensities in the spiral shock waves tend to be reduced compared to the case without mass-loss. Figure 9 illustrates the effects of mass-loss on the light curve produced from a kicked disk, as well as the luminosity produced in the mass-loss case.

The above estimates for the light-curve utilize only the effective dissipation that occurs, implicitly, in our simulations. The photons generated by this dissipation must escape the disk before they can be observed. We next use standard α -disk models to estimate the basic parameters of a more realistic disk. We adopt the equations describing the radial profile of the density, scale-height, temperature, and opacity of a standard thin accretion disk as summarized in Haiman et al. (2009b, based, in turn, primarily on Frank et al. 2002 and on Goodman & Tan 2004). In Figure 10, we show the temperature (T ; in Kelvin; green curves), the vertical optical depth (τ ; blue/red when electron scattering/free-free opacity dominates, respectively), the cooling time due to Bremsstrahlung emission (t_{cool} ; taken from eq. 6.53 in Frank et al. 2002 in units of seconds; magenta curves) and the vertical photon escape time (t_{esc} ; in units of days; black curves). The vertical optical depth is taken to be $\tau = \max(\tau_{\text{es}}, \tau_{\text{ff}})$, where τ_{es} is the free-free optical depth from Kramer’s opacity, and τ_{ff} is the electron scattering optical depth. The photon escape time is obtained as the product of the mean-free-path H/τ (where H is the vertical scale-height) and the number of scatterings in a random walk required to escape (τ^2), divided by the speed of light, $t_{\text{esc}} = (H/c)\tau$. All curves are for a $M = 10^6 M_\odot$ black hole. Solid curves are

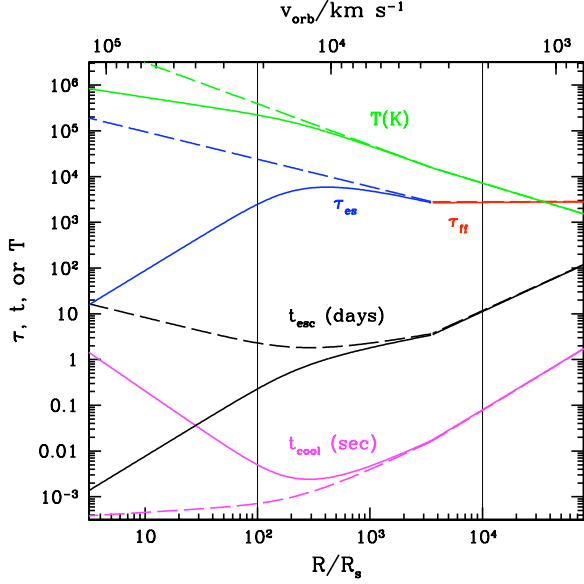


Figure 10. Physical quantities in a standard α -disk around a $M = 10^6 M_\odot$ black hole, as a function of radius (lower labels) and corresponding orbital velocity (upper labels). We show the temperature (T ; in Kelvin; green curves), the vertical optical depth (τ ; blue/red when electron scattering/free-free opacity dominates, respectively), the Bremsstrahlung cooling time (t_{cool} ; in units of seconds; magenta curves) and the vertical photon escape time (t_{esc} ; in units of days; black curves). Solid curves are for a standard α -disk (with viscosity scaling with total gas + radiation pressure), and the dashed curves are for a standard β -disk (with viscosity scaling with gas pressure). The thin vertical lines bracket the extent of the high-resolution mesh in our simulations.

for a standard α -disk (with viscosity proportional to the total pressure of gas + radiation), and the dashed curves are for a β -disk (with viscosity proportional to the gas pressure). The viscosity parameter, the accretion rate (in Eddington units), and the radiative efficiency were chosen to be $\alpha = 0.3$, $\dot{m} = 0.1 \dot{M}_{\text{Edd}}$ and $\epsilon = 0.1$, respectively. All the other parameters, which have a relatively minor effect on the profiles, are the same as the fiducial ones defined in Haiman et al. (2009b).

As Figure 10 shows, the disk is optically thick ($\tau \gg 1$) at all relevant radii, and at radii $\lesssim 8000 R_s$, the opacity is dominated by electron scattering. Near this radius, the local Bremsstrahlung cooling time is negligibly short, and the photon escape time from the disk is only ~ 3 days. Therefore, even though the disk is optically thick, the photons, generated by dissipation in the mid-plane, will emerge from the disk with a relatively short delay. These conclusions are derived for a steady disk. In the case of a binary, the pile-up of material near $100 R_s$ will modify the disk structure, corresponding, locally, to a non-accreting ($\dot{M} = 0$) disk (Ivanov, Papaloizou, & Polnarev 1999; Milosavljevic & Phinney 2005); however, the steady-disk model should give a good order-of-magnitude estimate farther out at $\sim 1000 R_s$, where the disk is relatively less disturbed before the merger.

Since the disk is very optically thick, the spectrum that emerges will be significantly processed, and close to a black-body shape (sometimes referred to as “grey-body”; e.g. Milosavljevic & Phinney 2005). Assuming for simplicity

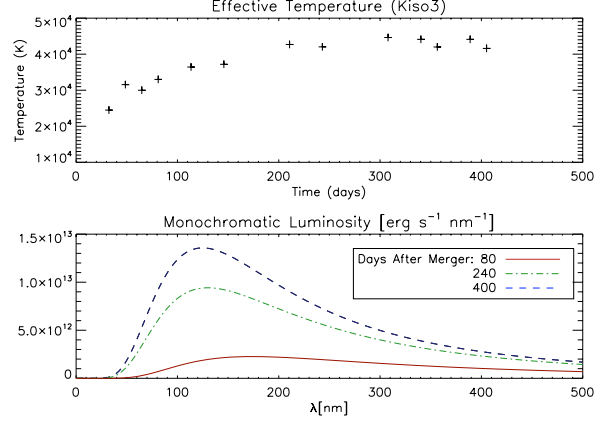


Figure 11. *Top panel:* effective black-body temperature T_{eff} for the most luminous point in the disk in the fiducial *Kiso3* run, defined by requiring the black-body surface brightness σT_{eff}^4 to equal the dissipation rate derived in the simulation. *Bottom panel:* total monochromatic luminosity emerging from our fiducial *Kiso3* disk at three different times, obtained by integrating the local black body emission over the face of the disk. The three curves (from bottom to top) show the spectra at $t = 80, 240,$ and 400 days after the merger.

that the radiation escaping from the surface has a perfect thermal spectrum, we can compute the required effective temperature T_{eff} , by equating the black-body luminosity per surface area σT_{eff}^4 to the luminosity density j we derive from the simulations. In the top panel of Figure 11, we show the evolution of this effective temperature, computed as a function of time at the most luminous point in the disk. As the figure shows, T_{eff} rises and asymptotes to $\sim 4.5 \times 10^4$ K, a value that is a factor of ~ 3 lower than the constant isothermal temperature T^{iso} imposed on the disk. This is consistent, to within a factor of \sim two, with the vertical structure in thin accretion disk models, in which the surface temperature is lower by a factor of $\sim \tau^{-1/4}$ than the mid-plane temperature (e.g. Frank et al. 2002).

From the similarity of the effective temperatures, we infer that the transient dissipation required to maintain a constant temperature in the disturbed disks is comparable (albeit an order of magnitude higher) than the viscous dissipation that occurs in a standard, steady-state, thin accretion disk. This implies that if the pre-merger disk luminosity was comparable to that of a thin accretion disk, the merger would be accompanied by an order-of-magnitude rise in luminosity. In practice, the total luminosity of a steady disk is dominated by its inner regions, and the pre-merger luminosity of the circumbinary disk can be significantly lower (and correspondingly, the merger will result in brightening by a much larger factor).

Interestingly, the monotonic rise in T_{eff} suggests that the shock-induced emission may have the unique signature of *hardening* in frequency by a factor of \sim two (in addition to monotonically rising in luminosity by a factor of a few) within the year following the merger event. In the bottom panel of Figure 11, we show the emergent composite spectrum, integrating the local black body emission over the face of the disk, which shows the same two features: the disk brightens, and the spectrum hardens with time. If confirmed by more accurate modeling of the emergent spectrum, this

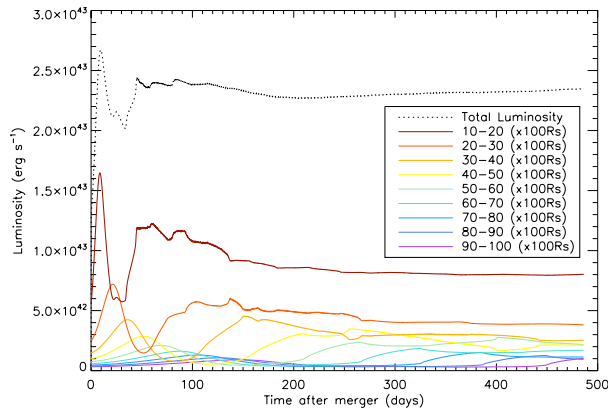


Figure 12. Total luminosity (black dotted line) compared to the luminosity contribution from different annuli (solid colored lines) in an α -disk that received a 530 km s^{-1} kick and experienced 5% mass loss from the central black hole (*MKiso*). The initial flares occur when the first two arms of the shock pass through the disk. However, the luminosity of the outer region of the shock decreases dramatically because less gas is swept up by the shocks in the outer regions of the disk, which is more diffuse. A large number of thin, tightly wound density waves persist throughout the entire disk, and the disk maintains a nearly constant luminosity until the end of the simulation.

should greatly help the identification of EM counterparts, since other types of known transient UV/optical/IR sources do not have these qualitative features.

3.4 Varying the Initial Disk Profile

All results in the previous sections are derived, for simplicity, for disks with constant initial density and temperature. In order to quantify the sensitivity of our results to the initial profiles, we have re-run several of our simulations with the power-law profiles in equations (1)-(3), approximating those in a more realistic, standard α -disk. The spatial resolution of all the α -disk run is set to be the same as in the highest-resolution constant density case, *Kiso3⁺⁺*, with $(\Delta r, \Delta\theta) = (5 R_s, 0.0025 \text{ rad})$. Table 2 summarizes the α -disk runs.

Figure 12 shows the total luminosity of the α -disk, again conservatively from the restricted region $10^3 < R/R_s < 10^4$ (black dotted line) together with the luminosity contribution from different annuli (solid colored lines). The first peak in each annulus, which is easily identifiable around $t = 10$ days in the $1000 < R/R_s < 2000$ bin, comes about when the first arm of the spiral shock forms. The second winding on the spiral arm, which is considerably narrower at early times than the first spiral arm, accounts for the second rise in the binned luminosity ($\sim t = 50$ days in the first bin). As the spiral pattern progresses outward, tighter windings of the spiral pattern persist and are generally long lasting due to the lack of viscous dissipation in the disk. As a result, after the first few windings of the spiral arm pass, each annulus contributes a steady background luminosity due to the numerous spiral density ripples that persist to the end of the simulation. While this is true in the uniform disk runs, as well, here the innermost annuli continue to dominate the total luminosity at all times, even though the outer annuli cover a larger surface area of the disk. It is

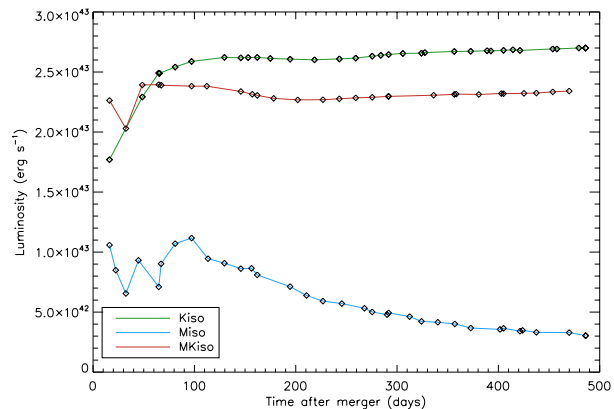


Figure 13. Light curves for three isothermal disks, experiencing kick and no mass-loss (*Kiso*), mass-loss and no kick (*Miso*), and both kick and mass-loss (*MKiso*) as in Figure 9, except the disks here have initial power-law density and temperature profiles, appropriate for a standard α -disk, rather than constant values. The luminosities rise more rapidly, due to the higher initial density concentration near the central regions, but settle at values similar to those reached in the constant density and temperature case.

also noticeable that, as the first few spiral arms propagate outward, their contribution contributes less and less to the total luminosity (compare Figure 12 to 8, where the flat portion of the lightcurve—contribution from each bin is due to the densest point moving into the respective region.) In the α -disk simulation, the front portion of the spiral shock contributes less to the total luminosity as it moves outward because the surface density of the gas is considerably lower at larger radii.

Figure 13 shows the light-curves in the three isothermal α -disk simulations. The absolute value of the luminosities arising from shocks in the α -disks is very close to the previous results in the constant density disk cases. However, there are a few qualitative differences worth noting. First, the luminosity rises more rapidly in the α -disks, reaching peak brightness in ≈ 100 days, compared to the constant-density disks, in which the peak is reached only after ≈ 300 days. While some of this more rapid rise can be attributed to the higher resolution employed for the α -disks, the resolution study in Figure 7 makes it clear that most of the difference is caused by the change in the profiles. This qualitative difference is unsurprising, since the α -disks are more centrally concentrated, and have more material in the inner regions, increasing the luminosities at early times. The mass-loss only case shows that a brighter and more prompt flare erupts after the merger, compared to the constant density disk; again this is attributable to the larger amount of material near the central regions. When both mass-loss and a kick is included, we find a prompt flare, followed by a nearly steady luminosity, reduced by around 15% from the kick-only case.

Overall, the light-curves in the α -disk and constant-density cases are reassuringly similar, indicating that variations in the assumed initial disk profiles do not lead to order-of-magnitude changes in the predicted brightness of the after-glow.

3.5 Numerical Issues

In this section, we discuss numerical effects from the inner and outer boundary of the simulation box, the dependence of our results on the spatial and time resolution, as well as numerically scaling our results to apply to black holes and disks with different physical sizes and kicks with different speeds.

Boundary conditions. Both at the inner and the outer boundaries, we imposed “outflow” boundary conditions that maintain a zero pressure and density gradient at the edges of the simulation. To test the effect of these boundary conditions, we checked whether an unperturbed disk (without any kick or mass-loss) maintains its uniform circular Kepler motion. We found that the outer disk, beyond $R_s = 10^3 R_s$, indeed remained undisturbed, but modest density ripples (with over-densities $\Sigma/\Sigma_i \lesssim 2$) were produced artificially inside $10^3 R_s$. The amplitude of these numerical fluctuations are below the density enhancements excited by shocks in the disk (see for example Figures 2 and 3). Nevertheless, this low-amplitude noise covers a large fraction of the surface area of the inner disk, and can dominate the total luminosity in the inner regions. This is a concern especially for the α disks, in which the inner regions were also found to dominate the total luminosity. More specifically, we computed the luminosity inside $R_s = 10^3 R_s$ in the unperturbed constant density and α -disk models, and we found that they reach values larger than (in the constant surface density disk cases) or comparable (in the α -disk cases) to the luminosities exhibited in the perturbed disks. In future work, we will attempt to identify the origin of this numerical noise, and to reduce its contribution to the luminosity. In the present paper, we simply derived luminosities outside $R > 10^3 R_s$, which are safe from numerical noise, but represent an underestimate the true total luminosity.

A separate concern is that due to the finite size of our simulation, the outermost regions of the spiral shock wave eventually reach the outer boundary of our region of interest. In the *Kiso3* run, the outer edge of the high-resolution mesh is reached at $t \approx 250$ days. Although the spiral shocks are subsequently still present farther out in the low-resolution mesh, we have excluded these poorly resolved shocks from our analysis and results. For example, the dense spiral arms moving out of the simulation box produce the turn-over in the percentage of the disk undergoing a shock, shown in Figure 4 (the figure only includes shocked gas within $R < 10^4 R_s$).

Numerical resolution. In order to test the numerical convergence of our results, we re-computed the light-curves in our fiducial disk (*Kiso3*) at a factor of two lower (*Kiso3⁻*) and factors of two and four higher (*Kiso3⁺* & *Kiso3⁺⁺*) spatial resolutions. Note that FLASH chooses time steps adaptively, matched to the spatial resolution, so each resolution test differs from the next by a factor of two in the time step, as well. The four curves in Figure 7 show the light-curves in each of these four runs, corresponding, from bottom to top, to increasing resolution. The light-curves begin to converge, in the sense that their fractional difference between pairs of resolutions begins to decrease. There is still a noticeable difference (by a relatively small fraction of $\approx 10\%$) between the luminosities computed in our highest and next-to-highest resolution run. Given that the total luminosity

is dominated by sharp features, it is not surprising that the disks are more luminous in the higher resolution runs – the density spikes are better resolved in these runs. At our fiducial resolution, the luminosities are underestimated by $\gtrsim 35\%$. Unfortunately, the computational time required to run the highest resolution simulations (which took approximately 2 weeks on 80 processors) was prohibitively expensive, and prevented us from further increasing our resolution, in order to achieve full convergence. However, the 10% difference between the two highest resolution runs is modest in comparison to other uncertainties arising from the highly idealized nature of our luminosity estimates. The resolution study also shows that our somewhat under-resolved simulations are conservative, underestimating the true luminosity.

Scaling simulation runs to physical units. The physical scales in each simulation are fixed by specifying the physical values of any two independent dimensional parameters – these can be taken to be the BH mass M , and the kick velocity v_{kick} . Our runs can describe systems with different combinations of BH masses and kick velocities, provided the other parameters are suitably adjusted. Consider the quantity X , specified in the simulations by a dimensionless value X^{sim} . The physical value X^{phys} of this quantity can be obtained by a constant conversion factor f , and will scale with M and v_{kick} as

$$\frac{X^{\text{phys}}}{X^{\text{sim}}} = f \left(\frac{M}{10^6 M_\odot} \right)^{\gamma_m} \left(\frac{v_k}{530 \text{ km/s}} \right)^{\gamma_v}. \quad (4)$$

Table 3 shows the factor fX^{sim} for various parameters specified in the initial condition of our fiducial run, and the mass- and velocity-dependence of these parameters; we also show the mass- and velocity-dependence of the physical luminosity and energy, derived from the simulations. For example, as v_{kick} increases, v_{orb} must increase in proportion, decreasing both the distance ($\propto v_{\text{kick}}^{-2}$) and time ($\propto v_{\text{kick}}^{-3}$) scales. Thus, our results would be applicable, for example, for $M = 10^6 M_\odot$ and $v_{\text{kick}} = 10^3 \text{ km s}^{-1}$, but would then describe the evolution of a 4 times smaller disk, with an inner cavity of size $25R_s$, and for only ≈ 50 days, rather than a year. The disks would also be 4 times hotter, and 16 times more massive than for the fiducial 530 km s^{-1} kick. The luminosity has the especially steep dependence $\propto v_{\text{kick}}^5$, so that higher-velocity kicks would be much more observable (provided, of course, that the scaled physical parameters are realized in nature). Other combinations to which our runs can correspond can be read off similarly from Table 3.

3.6 Comparison with Previous Work

Lippai et al. (2008) considered the response of a collisionless disk to kicks. Qualitatively, the spiral shock structures shown in Figure 1 in our fiducial *Kiso3* run are very similar to the caustics shown in Figure 1 of Lippai et al. (2008) for a system with the same parameters (the only difference is that Lippai et al. 2008 used $v_{\text{kick}} = 500 \text{ km s}^{-1}$). However, a more quantitative comparison is useful to separate hydrodynamical effects from those arising from orbital dynamics.

Figure 3 shows the radial position of the densest point in the simulated disks, compared to the location r_c of the outermost caustic identified in a collisionless case (Lippai et al. 2008). The straight dotted lines correspond to propagation at constant speeds of $v_{\text{kick}} = 530 \text{ km s}^{-1}$ (lower

Table 3. Conversion from the physical parameters in our fiducial run to other values, for each parameter specified in our initial conditions, as well as for the luminosity and energy derived from the simulations.

Simulation Parameter	Conversion Factor (fX^{sim})	γ_m	γ_v
BH Mass (M_\odot)	10^6	1	0
Radius of inner disk edge (cm)	3.0×10^{13}	1	-2
Maximum time (days)	500	1	-3
Kick velocity (km s^{-1})	530	0	1
Gas temperature (K)	1.4×10^5	0	2
Surface Density (g cm^{-2})	1.5×10^5	-1	4
Luminosity (erg s^{-1})	–	0	5
Energy (erg)	–	1	2

line) and $2v_{\text{kick}} = 1060 \text{ km s}^{-1}$ (upper line). As the figure demonstrates, the shocks found in our isothermal runs form at locations very close to those of the collisionless caustics. Both follow the approximate simple linear expansion $r_c \approx v_{\text{kick}}t$ expected from the epicyclic approximation (Lippai et al. 2008), although the propagation is somewhat faster at early times, and somewhat slower at late times. Apparently, while the temperature has a strong impact on the overdensities and the strengths of the shocks (shown, e.g., in Fig. 2) it makes a comparatively small difference to their propagation speed or to their overall morphology. These results also provide reassurance that the shock propagation was not affected by numerical edge effects from the inner and outer boundary of the simulation. Interestingly, on the other hand, the equation of state has a significant impact, with the propagation \sim twice as rapid in the adiabatic runs. As mentioned above, this apparent difference in the propagation speed of the densest point arises partly because the densest point falls further out along the outermost spiral arm in the adiabatic runs, and partly because the gas pressure makes the outermost spiral arms more diffuse and extend to a larger radius.

As mentioned in § 3.1 above, we found that pressure suppresses density enhancements in the disk at late times, by large factors. This last conclusion is somewhat surprising, given expectations from collisionless disks. Lippai et al. (2008) found that the relative velocity v_c of particles, as they cross on their orbits to create the caustics, increases with increasing radius as $v_c \sim v_{\text{kick}}^2/v_{\text{orbit}} \propto r^{1/2}$ (where v_{orbit} is the orbital velocity). The collisions therefore become super-sonic beyond some critical radius; this critical radius typically lies within the range of radii shown in Figure 2. For example, in the fiducial run *Kiso3*, the critical radius is at $1,300R_s$, and in the higher-temperature runs *Kiso4* and *Kiso5*, it is at $4,200R_s$ and $13,000R_s$, respectively. We find that the large overdensity of the shocks can be attributed to “pre-compression”. In particular, the shocks exceed the overdensity of a factor of 4 relative to the surface density at the start of the simulations. This is because significant overdensities start building up along the spiral pattern before the actual shocks occur. This increases the absolute density of the shock, since the shock is hitting gas that already has a surface density higher than the initial value. For example, in Figure 1, the adiabatic simulation (*Kad3*) shows that the outermost edge of the spiral pattern has overdensities forming with $\Delta\Sigma \approx 2$. For a strong shock and $\gamma = 5/3$, we

expect a density enhancement about 4 times that of the initial density, or $\Sigma \approx 8\Sigma_i$, which is what we see in the denser part of the spiral. A similar mechanism is at work in the isothermal simulation (*Kiso3*), but the shocked gas is able to cool and reach much larger densities. This pre-compression, which happens on time-scales much longer than the shock-formation itself, can apparently be significantly suppressed by gas pressure.

Lippai et al. (2008) also proposed that the shock temperature scales with time/radius as $T_{\text{shock}} \propto v_c^2 \propto v_{\text{orbit}}^{-2} \propto r_c \propto t_c$, and suggested that the luminosity is dominated by the outermost shocked shells, with both the total luminosity and the characteristic frequency of the emitted spectrum increasing with time. The same qualitative behavior is seen in our isothermal, constant-density simulations. However, we find that the largest Mach number in the spiral arms increases from $\mathcal{M} = 1.7$ to $\mathcal{M} = 3$, between $t = 16$ and 310 days, much less steeply than linearly with time (and radius). In our adiabatic runs, the Mach numbers decline from 2 to 1.1 in the same interval. This decline, however, is due to the increase in sound speed, rather than a decrease in the gas velocities.

Assuming a disk profile with $\Sigma \propto r^{-3/5}$ (close to the one adopted in our α -disk runs), and also that a constant fraction of the disk mass interior to the outermost spiral caustic is shocked ($M_{\text{shock}} \propto \Sigma r dr$) and that the energy is released over the time-scale of $t_c = r_c/v_{\text{kick}}$, Lippai et al. (2008) also finds the scaling $L_{\text{kick}} \approx (1/2)M_{\text{shock}}v_c^2/t_c \propto r^{19/10}$. As discussed in § 3.3 above, the disk is likely to be optically thick, in which case the spectrum is significantly re-processed, invalidating naive conclusions about the optically-thin spectrum. In the constant-density runs, we nevertheless find an approximately linearly rising luminosity, and also a modestly increasing characteristic frequency. While this is in qualitative agreement with the above expectations, most of the rise in the luminosity in our case is explained by the increasing fraction of the disk mass that is shocked, with the increase in the characteristic temperature contributing relatively little. In our α -disk runs, we find a light-curve that initially rises and then reaches a nearly constant luminosity after ≈ 100 days.

As mentioned in the Introduction, O’Neill et al. (2009) and Megevand et al. (2009) have recently employed three-dimensional simulations to study the evolution of much smaller disks (extending from $2 - 50R_s$ and $10 - 30R_s$, respectively, compared to our $10^2 - 10^4R_s$) on much shorter

time-scales (~ 5 hrs and ~ 6 hrs, scaling to a $10^6 M_\odot$ BH; compared to our ~ 500 days). Since our FLASH simulation results are output at times that sample the disk evolution only every ≈ 4 days, we can not directly compare the behavior of our disks to those in O’Neill et al. (2009) and Megevand et al. (2009).

Despite the mis-match in scales and different dimensionality, it is interesting to contrast the light-curves we find here with those in O’Neill et al. (2009) and Megevand et al. (2009). We first note that the simulations in both O’Neill et al. (2009) and Megevand et al. (2009) are adiabatic, i.e., they are energy-conserving by construction. O’Neill et al. (2009) and Megevand et al. (2009) present estimates for the luminosity by computing the volume-integral of the quantity $\rho^2 T^{1/2}$, which is proportional to the local Bremsstrahlung emissivity. As we discussed in § 3.3 above, the Bremsstrahlung cooling time is exceedingly short, so if dissipation indeed tracked the Bremsstrahlung emission, the adiabatic condition could not be maintained. If cooling were efficient, then one expects, instead, much stronger overdensities to develop than in the adiabatic case, which would, in turn, generically increase the cooling rate $\propto \int dV \rho^2 T^{1/2}$.

Setting these inconsistency issues aside, in order to compare our results as directly as possible to O’Neill et al. (2009) and Megevand et al. (2009), we computed the quantity $L_{\text{Brem}} = \int dV \rho^2 T^{1/2}$ in both our adiabatic and isothermal simulations. Unfortunately, this comparison is further complicated by the fact that our simulations are two-dimensional. In order to calculate the 3D gas densities and volume elements, ρ and dV from the constant density disks, we assumed that the disk has the scale height $H = c_s/\Omega$ obtained by assuming hydrostatic equilibrium in the vertical direction (here $c_s = \sqrt{kT/\mu m_p}$ and $\Omega = v_\phi/r$ are measured directly in the simulation run). This assumption should be reasonable, since we simulated $N \gg 1$ dynamical times, except near the outer edge of the disk. Note that if hydrostatic equilibrium was not established (i.e. the disk was still expanding in the vertical direction, following the mass-loss or recoil), the disk would be thinner, and the 3D densities would be even higher than our estimates, increasing the predicted luminosities. Finally, note that under the assumption of hydrostatic equilibrium, and with $\rho = \Sigma/H$, the Bremsstrahlung integral becomes independent of temperature, $\int dV \rho^2 T^{1/2} = \text{const} \int dr \Sigma^2 r^{-1/2}$.

The solid curve in bottom panel in Figure 14 shows the evolution of L_{Brem} in the mass-loss only, constant density disk runs. The light curve exhibits oscillations within the first 100 days after the merger, qualitatively similar to the dips and troughs found, on shorter time-scales, by both O’Neill et al. (2009) and Megevand et al. (2009). In particular, as in the those two studies, the entire disk remains dimmer than prior to the mass-loss: the luminosity of the disk decays by $\approx 20\%$ over the course of a year. To understand this result better, we computed the time-dependent mean surface density $\langle \Sigma \rangle$ of the simulated disk between $10^3 - 10^4 R_s$. As noted above, the disk as a whole expands after the mass-loss, due to the sudden decrease in gravitational force from the central point mass. We show, by the dashed curve in the bottom panel of Figure 14, the Bremsstrahlung luminosity that would result from a disk with the time-dependent surface density $\langle \Sigma \rangle_t$. The departure of the dashed curve from unity is therefore due entirely to changes in the

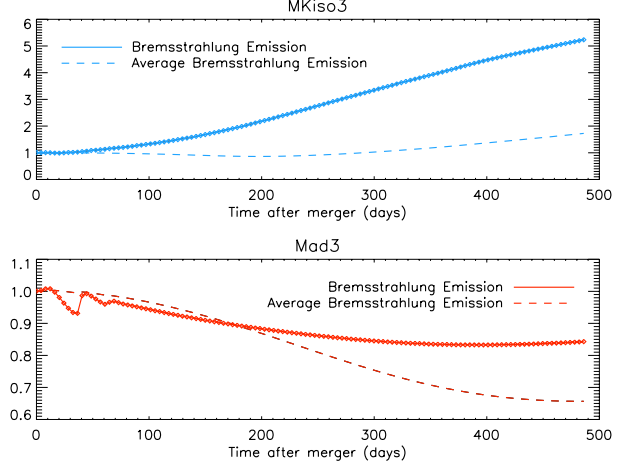


Figure 14. *Lower panel:* Thermal Bremsstrahlung emission from an adiabatic, constant-density disk that experiences the effect of 5% mass loss and no kick (*Mad3*). The luminosity is normalized to its steady pre-merger value. Initially, the light curve exhibits variability, qualitatively similar to the dips and troughs found, on shorter time-scales, by both O’Neill et al. (2009) and Megevand et al. (2009). The dashed curve shows, for comparison, the Bremsstrahlung luminosity that would result from a disk with uniform surface density and the same total mass. The prominent dip at $t > 100$ days is caused by $\approx 20\%$ of the original disk material exiting the simulation volume. *Upper panel:* Bremsstrahlung emission from our fiducial isothermal disk, experiencing both mass-loss and a kick (*MKiso3*). The dashed curve shows the corresponding luminosity from a uniform disk, as in the lower panel. The disk brightens, mostly due to the sharp density contrasts that develop.

total disk mass within the region $10^3 - 10^4 R_s$, whereas the difference between the solid and dashed curve is caused entirely by inhomogeneities in the gas surface density in this region. As these two curves show, at early times, the drop in the luminosity is due mostly to inhomogeneities, whereas at late times, the dimming is caused by approximately 20% of the disk mass exiting the simulated region. Note that at late times, the inhomogeneities actually cause an increase in the luminosity. At early times, inhomogeneities cause the luminosity to decrease. While naively one expects that inhomogeneities always boost the luminosity, we note that in the adiabatic case, the disk is effectively allowed to expand in the vertical direction, and inhomogeneities can cause a small overall decrease in the luminosity.

In comparison, the top panel in Figure 14 shows L_{Brem} in our fiducial isothermal run (*Kiso3*), which includes both a kick and a mass-loss. As in the bottom panel, the dashed curve shows the luminosity from a uniform disk with the same total mass. As this figure shows, the luminosity significantly *increases* with time, and this increase is mostly due to the inhomogeneities (note that the density contrasts are much higher than in the adiabatic case, and the isothermal disk does not expand in the vertical direction). Interestingly, in this run that includes the kick, the total mass within the $10^3 - 10^4 R_s$ region increases, rather than decreases.

In summary, our constant-density, adiabatic disks, which include only mass-loss and no kick, show the same qualitative behavior as in O’Neill et al. (2009) and Megevand et al. (2009), namely oscillations in the luminosity, and

a modest overall dimming of the disk, following the BH merger. However, using an isothermal, rather than an adiabatic equation of state and considering the impact of a kick, in addition to the mass-loss, tend to counter this dimming, and when combined, produce, instead a significant brightening of the disk - due mostly to the stronger density contrasts that develop in the isothermal case.

4 CONCLUSIONS AND FUTURE DIRECTIONS

In this paper, we used two-dimensional hydrodynamical simulations of a circumbinary disk, to follow the effects of a velocity recoil and mass-loss of the central black hole binary, following the merger of the two black holes. From a suite of runs, we are able to draw two basic conclusions.

First, the outward-propagating spiral shocks that develop in our simulations follow a pattern very similar to the caustics identified in collisionless disk (Lippai et al. 2008). Gas pressure has a modest overall impact on the propagation and on the overall morphology of the shocks. On the other hand, we find that the gas pressure, and the assumed equation of state, has a strong impact on the overdensities that develop and on the strengths of the shocks: isothermal, low-temperature disks have larger overdensities and stronger shocks.

Second, we have estimated an upper limit on the luminosity emerging from the disk experiencing a BH kick with $v_{\text{kick}} = 530 \text{ km s}^{-1}$, by measuring the effective dissipation that occurs, implicitly, in the simulations when an isothermal condition is imposed on the gas. The resulting luminosity is of order 10% of the Eddington limit for the $10^6 M_{\odot}$ BH used in the simulation, which suggests that the after-glow may be bright enough to be detectable. If the pre-merger disk has a luminosity below that of a standard steady-state thin accretion disk (due to the evacuation of the inner regions of the disk), then the merger-induced kick will cause a significant (order-of-magnitude, or larger) brightening of the disk. We also estimated the effective black-body temperature of the radiation emerging from the optically thick disk. We found that as the disk brightens, the characteristic frequency increases with time, possibly offering a unique signature of the kick-induced emission. When the accompanying mass-loss of the merger remnant is included in our simulations, the density contrasts and luminosity from the spiral shocks decrease somewhat, but do not change dramatically in overall behavior.

While our results are encouraging, and suggest that the EM signature of the disturbed circumbinary disk may be detectable, this conclusion has to be verified in the future in improved models. In particular, a better estimate of the thermodynamics of the disk, with a realistic treatment of radiative cooling, should reveal how close the luminosity is to the values we obtained here, using the isothermal assumption; by using three-dimensional simulations that resolve the vertical disk structure, and by following the vertical transfer of the radiation produced should clarify the robustness of our conclusions about the evolution of the characteristic emergent frequency.

5 ACKNOWLEDGMENTS

We are grateful to Kristen Menou, Mordecai MacLow, Greg Bryan, and Bence Kocsis for useful discussions. The software used in this work was in part developed by the DOE-supported ASCI/Alliances Center for Astrophysical Thermonuclear Flashes at the University of Chicago. This work was supported by the Polányi Program of the Hungarian National Office for Research and Technology (NKTH) and by the NASA ATFP grant NNX08AH35G.

REFERENCES

- Armitage, P. J., & Natarajan, P. 2002, *ApJ*, 567, L9
 Artymowicz, P., & Lubow, S. H. 1994, *ApJ*, 421, 651
 Artymowicz, P., & Lubow, S. H. 1996, *ApJ*, 467, L77
 Baker, J. G., Centrella, J., Choi, D.-I., Koppitz, M., van Meter, J. R., & Miller, M. C. 2006, *ApJ*, 653, L93
 Baker, J. G., Boggs, W. D., Centrella, J., Kelly, B. J., McWilliams, S. T., Miller, M. C., & van Meter, J. R. 2007, *ApJ*, 668, 1140
 Baker, J. G., Boggs, W. D., Centrella, J., Kelly, B. J., McWilliams, S. T., Miller, M. C., & van Meter, J. R. 2008, *ApJL*, 682, L29
 Barnes, J. E. 2002, *MNRAS*, 333, 481
 Bekenstein, J. D. 1973, *ApJ*, 183, 657
 Bloom, J. S. et al. 2009, *Astro2010 Decadal Survey White Paper*, e-print arXiv:0902.1527
 Bogdanović, T., Reynolds, C. S., & Miller, M. C. 2007, *ApJL*, 661, L147
 Campanelli, M., Lousto, C. O., Zlochower, Y., & Merritt, D. 2007a, *ApJ*, 659, L5
 ——— 2007b, *Phys. Rev. Lett.*, 98, 231102
 Cuadra, J., Armitage, P. J., Alexander, R. D., & Begelman, M. C. 2009, *MNRAS*, 393, 1423
 Deffayet, C., & Menou, K. 2007, *ApJL*, 668, L143
 Dotti, M., Salvaterra, R., Sesana, A., Colpi, M., & Haardt, F. 2006, *MNRAS*, 372, 869
 Escala, A., Larson, R. B., Coppi, P. S., & Mardones, D. 2005, *ApJ*, 630, 152
 Fitchett, M. J. 1983, *MNRAS*, 203, 1049
 Frank, J., King, A., & Raine, D. J. “Accretion Power in Astrophysics: Third Edition,” 2002, Cambridge University Press, ISBN 0521620538
 Fryxell, B., et al. 2000, *ApJS*, 131, 273
 Goodman, J. & Tan, J. C. 2004, *ApJ*, 608, 108
 González, J. A., Spherhake, U., Brüggmann, B., Hannam, M. D., & Husa, S. 2007a, *Phys. Rev. Lett.*, 98, 091101
 González, J. A., Hannam, M. D., Spherhake, U., Brüggmann, B., & Husa, S. 2007b, *Phys. Rev. Lett.*, 98, 231101
 Haiman, Z., Kocsis, B., Menou, K., Lippai, Z., & Frei, Z. 2009a, *Classical and Quantum Gravity*, 26, 094032
 Haiman, Z., Kocsis, B., & Menou, K. 2009b, *ApJ*, in press, e-print arXiv:0904.1383
 Hayasaki, K. 2009, *PASJ*, 61, 65
 Hayasaki, K., Mineshige, S., & Ho, L. C. 2008, *ApJ*, 682, 1134
 Hayasaki, K., Mineshige, S., Sudou, H. 2007, *PASJ*, 59, 427
 Herrmann, F., Hinder, I., Shoemaker, D., Laguna, P., & Matzner, R. A. 2007a, *ApJ*, 661, 430
 ——— 2007b, *Phys. Rev. D*, 76, 084032

- Herrmann, F., Hinder, I., Shoemaker, D., & Laguna, P. 2007c, *Class. Quant. Gr.*, 24, 33
- Holz, D. E., & Hughes, S. A. 2005, *ApJ*, 629, 15
- Ivanov, P. B., Papaloizou, J. C. B., & Polnarev, A. G. 1999, *MNRAS*, 307, 79
- Kocsis, B., Frei, Z., Haiman, Z. & Menou, K. 2006, *ApJ*, 637, 27
- Kocsis, B., Haiman, Z., Menou, K., & Frei, Z. 2007, *Phys. Rev. D.*, 76, 2003
- Kocsis, B., Haiman, Z., & Menou, K. 2008, *ApJ*, 684, 870
- Koppitz, M., Pollney, D., Reisswig, C., Rezzolla, L., Thornburg, J., Diener, P., & Schnetter, E. 2007, *Phys. Rev. Lett.* 99, 041102
- Lang, R. N., & Hughes, S. A. 2008, *ApJ*, 677, 1184
- Lippai, Z., Frei, Z., & Haiman, Z. 2008, *ApJL*, 676, L5
- Liu F. K., Wu X.-B., & Cao S.L. 2003, *MNRAS*, 340, 411
- MacFadyen, A. I., & Milosavljević, M. 2008, *ApJ*, 672, 83
- Megevand, M., Anderson, M., Frank, J., Hirschmann, E. W., Lehner, L., Liebling, S. L., Motl, P. M., & Neilsen, D. 2009, *Phys. Rev. D*, submitted, e-print arXiv:0905.3390
- Milosavljevic, M., & Phinney, E. S. 2005, *ApJ*, 622, L93
- O’Neill, S. M., Miller, M. C., Bogdanovic, T., Reynolds, C. S., & Schnittman, J. 2008, *ApJ*, in press, arXiv:0812.4874
- Phinney, E. S. 2009, *Astro2010 Decadal Survey White Paper*, e-print arXiv:0903.0098
- Schnittman, J. D., & Krolik, J. H. 2008, *ApJ*, 684, 835
- Shields, G. A., & Bonning, E. W. 2008, *ApJ*, 682, 758
- Tichy, W., & Marronetti, P. 2008, *Phys. Rev. D.*, 78, 081501
- Vecchio, A. 2004, *Phys. Rev. D.*, 70, 042001